pdfauthor=I. E. M. de Graaf et al. pdftitle=A high resolution global scale groundwater model title Manuscript prepared for Hydrol. Earth Syst. Sci. Discuss.
with version 4.1 of the LaTeX class copernicus_discussions.cls.
Date: 24 September 2014

A high resolution global scale groundwater model

I. E. M. de Graaf[1], **E. H. Sutanudjaja**[1], **L. P. H. van Beek**[1], **and M. F. P. Bierkens**[1,2]

[1]Department of Physical Geography, Faculty of Geosciences, Utrecht University, Utrecht, the Netherlands
[2]Unit Soil and Groundwater Systems, Deltares, Utrecht, the Netherlands

Correspondence to: I. E. M. de Graaf (i.e.m.degraaf@uu.nl)

Abstract

abstr Groundwater is the world's largest accessible source of fresh water. It plays a vital role in satisfying basic needs for drinking water,agriculture and industrial activities. During times of drought groundwater sustains baseflow to rivers and wetlands, thereby supporting ecosystems. Most global scale hydrological models (GHMs) do not include a groundwater flow component, mainly due to lack of geohydrological data at the global scale. For the simulation of lateral flow and groundwater head dynamics a realistic physical representation of the groundwater system is needed, especially for GHMs that run at finer resolutions. In this study we present a global scale groundwater model (run at 6′ resolution) using MODFLOW to construct an equilibrium water table at its natural state as the result of long-term climatic forcing. The used aquifer schematization and properties are based on available global datasets of lithology and transmissivities combined with estimated aquifer thickness of an upper, unconfined aquifer. The model is forced with outputs from the land-surface model PCR-GLOBWB, specifically with net recharge and surface water levels. A sensitivity analysis, in which the model was run with various parameter settings, showed variation in saturated conductivity causes most of the groundwater level variations. Validation with observed groundwater heads showed that groundwater heads and depths are reasonably well simulated for many regions of the world, especially for sediment basins ($R^2 = 0.95$). The simulated regional scale groundwater patterns and flowpaths demonstrate the relevance of taking lateral groundwater flow into account in GHMs. The resulting inter-basin groundwater flows can be a significant part of a basin's water budget and helps to sustain river baseflows, explicitly during times of droughts. Also, water availability of larger aquifer systems can be positively affected by additional recharge from inter-basin groundwater flows.

1 Introduction

Groundwater is a crucial part of the global water cycle. It is the world's largest accessible source of fresh water and plays a vital role in satisfying basic needs of human society. It is a primary source for drinking water and supplies water for agriculture and industrial activities (Wada et al.,

2014). During times of drought stored groundwater provides a buffer against water shortage and sustains baseflow to rivers and wetlands, thereby supporting ecosystems and biodiversity. However, in many parts of the world groundwater is abstracted at rates that exceed groundwater recharge, causing groundwater levels to drop while baseflows to rivers are no longer sustained (Konikow, 2011; Gleeson et al., 2012).

In order to understand how groundwater dynamics are affected by variations in recharge and human water use, lateral groundwater flow and groundwater surface water interactions should be included in global scale hydrological models (GHMs), especially as these GHMs progressively move towards finer resolutions (Wood et al., 2012; Krakauer et al., 2014). Several studies (e.g. Bierkens and van den Hurk, 2007; Fan et al., 2007) have suggested that lateral groundwater flows can be important for regional climate conditions as it influences soil moisture and thus the water cycle and energy exchange between land and the lower atmosphere. Moreover, inter- basin groundwater flow can be a significant part of the water budget in a river basin under certain climate and geological conditions (Schaller and Fan, 2009); it positivity contributes to sustain river baseflows during times of droughts positively affecting ecosystems and wetlands and increasing surface water availability for human water use (de Graaf et al., 2014). Also, large aquifer systems are additionally recharged by inter-basin groundwater flow, which has a positive influence on water availability for groundwater abstraction.

Up to now, the current generation of GHMs typically does not include a lateral groundwater flow component mainly due to the lack of worldwide hydrogeological information (Gleeson et al., 2014). These data are available for parts of the developed world, but even there it is difficult to obtain data in a consistent manner. To cope with the unavailability of hydrogeological data Sutanudjaja et al. (2011) proposed the use of global datasets of surface lithology and elevation for aquifer parameterization. This method was tested by building a groundwater flow model for the Rhine–Meuse basin ($30''$ resolution) with promising results. Similarly, Vergnes et al. (2012) used global and European datasets to delimit the main aquifer basins for France (at 0.5° resolution) and parameterized them on lithological information for France.

Recently, a pioneering study by Fan et al. (2013) presented a first ever high-resolution global groundwater table depth map. Their method however, does not include hydrogeological infor-

mation such as aquifer depths and transmissivities, but uses estimates from soil data. Also, the hydraulic connection between rivers and groundwater, which is the primary drainage for groundwater in humid regions, is ignored. Also, their model requires calibration to head observations.

In this paper we present a global-scale groundwater model of an upper aquifer which is assumed to be unconfined. For the parameterization of the aquifer properties we relied entirely on available global lithological maps (Hartmann and Moosdorf, 2012) and databases on permeability (Gleeson et al., 2011). To overcome the lack of information about aquifer thickness worldwide, this is estimated based on extrapolation of available data from the USA. This can equally be extended to data-poor environments.

We forced the groundwater model with output from the global hydrological model PCR-GLOBWB (van Beek et al., 2011), specifically the net groundwater recharge and average surface water levels derived from routed channel discharge. This approach builds on earlier work by Sutanudjaja et al. (2011) and Sutanudjaja et al. (2014).

With this approach we were able to simulate groundwater heads of a upper unconfined aquifer, providing a first-order estimate of the spatial variability of water table heads as a function of climate and geology. In this paper we limit ourselves to a steady-state simulation as a prelude to transient simulations in forthcoming work. Also we did not yet perform a formal calibration of the model. We performed a sensitivity analysis using a Monte Carlo framework in which we ran the model with various hydrogeological parameter settings. Simulated groundwater heads from all realizations were validated against reported piezometer data and the parameter set with the highest coefficient of determination was used for further analysis. This resulted in a global map of average groundwater table depth in its natural state, i.e. in equilibrium with climate and without groundwater pumping. We simulated flowpaths to show the actual path through the subsoil that the groundwater follows from the location of infiltration towards the location of drainage. Flowpaths show areas where lateral groundwater flows are important and inter-basin groundwater flows are significant and contribute to water availability in neighbouring watersheds. They also provide an indication of groundwater travel times.

Hereafter follows a description of the methods, in particular the parameterization of the upper aquifer, after which results of the sensitivity analysis and validation are presented. Next, the groundwater table depth map and flowpath maps for Europe and Africa are presented. We end with conclusions and discussion.

2 Methods

2.1 General

The hydrological model of the terrestrial part of the world (excluding Greenland and Antarctica) developed in this study consists of two parts; (1) the dynamic land surface model (PCR-GLOBWB) and (2) the steady state groundwater model (MODFLOW). Both the land-surface model and groundwater model are run at $6'$ resolution (approximately 11 km at the equator). PCR-GLOBWB and MODFLOW are coupled offline where both models are run consecutively (Sutanudjaja et al., 2011).

2.1.1 Land surface model

The model PCR-GLOBWB is a global hydrological model that simulates hydrological processes in and between two soil stores and one underlying linear groundwater store. For a detailed description of the model PCR-GLOBWB we refer to van Beek et al. (2011), and a summarized model description is given here. PCR-GLOBWB was run at $6'$ resolution using a daily time step. Monthly climate data were taken from the CRU TS2.1 (Mitchell and Jones, 2005) with a spatial resolution of 0.5° and downscaled using the ERA-40 (Uppala et al., 2005) and ERA-Interim reanalysis (Dee et al., 2011) to obtain a daily climatic forcing (see de Graaf et al. (2014) for a more detailed description of this forcing dataset). Each grid-cell contains a land surface that is represented by a vertical structured soil column comprising two soil layers (maximum depth 0.3 m and 1.2 m respectively), an underlying groundwater reservoir, and the overlying canopy. Sub-grid variability is included with regards to land cover (in this case using fractions of short and tall vegetation),soil conditions, and topography. The model employs the improved

Arno Scheme (Todini et al., 1996; Hagemann et al., 1999) to simulate variations in the fraction of saturated soil in order to quantify direct surface runoff. For each time step and for every grid cell the water balance of the soil column is calculated on the basis of the climatic forcing that imposes precipitation, reference-crop potential evapotranspiration, and temperature. Actual evapotranspiration is calculated from reference-crop potential evaporation, time-varying crop-factors, and soil moisture conditions. Vertical exchange between the soil and groundwater occurs through percolation and capillary rise. Specific runoff from the soil column, comprising direct surface runoff, interflow, and baseflow, is accumulated along the drainage network that consists of laterally connected surface water elements representing river channels, lakes or reservoirs. The accumulated runoff is routed to obtain discharge using the kinematic wave approximation of the Saint-Venant equations at a sub-daily time step. In the original version of PCR-GLOBWB no lateral groundwater flow is simulated. Groundwater flow within a cell is described as a linear store and recharge is simulated as percolation to the groundwater store, minus capillary rise from the groundwater store to the soil. However, in the current set-up, the capillary rise is disabled to force a one-way coupling from PCR-GLOBWB to MODFLOW.

2.1.2 Groundwater model

In this study the linear groundwater store of PCR-GLOBWB is replaced by a MODFLOW layer (McDonald and Harbaugh, 2000; Schmitz et al., 2009) simulating lateral groundwater flows and groundwater heads in a single-layer unconfined aquifer. Aquifer properties are prescribed and the MODFLOW layer is forced by outputs from PCR-GLOBWB, i.e. long-term averages of surface water levels and groundwater recharge (running period 1960-2010). Figure 1 illustrates the modelling strategy.

2.2 Estimating aquifer properties

Aquifer properties were initially based on two datasets; (1) the high resolution global lithological map (GLiM) of Hartmann and Moosdorf (2012), and (2) the global permeability estimates of Gleeson et al. (2011).

The GLiM describes 16 lithology classes (similar and expending on Dürr et al., 2005). It is assumed that the lithological map represents the geology of the shallow subsurface accurately (Hartmann and Moosdorf, 2012). For the global permeability map the lithology classes of Dürr et al. (2005) were paired to 5 combined hydrolithologies, representing broad lithologic categories with similar hydrogeological characteristics (Gleeson et al., 2011). In the GLiM, these hydrolithological units were subsivided further on the basis of texture in the case of unconsolidated and sedimentary rocks (Table 1). (Gleeson et al., 2011) found that for all hydrolithologies permeability is representative for larger scales and that there is no discernible additional dependence of permeability on scale, with the exception of carbonates, most likely due to karst. The resulting map shows regional scale permeability over the globe with the geometric mean permeability attributed to each hydrolithological unit. The geometric mean was obtained from calibrated permeabilities from groundwater models for units larger than $5\,\mathrm{km}$ in extent within $100\,\mathrm{m}$ depth. The polygons in the GLiM,delineating a hydrological unit, were subsequently gridded to $30''$ ($\sim 1\,\mathrm{km}$) and aggregated as the geometric mean at $6'$ resolution.

To estimate aquifer transmissivities (kD in $\mathrm{m^2\,d^{-1}}$), aquifer thicknesses are required. Since no globally consistent dataset on aquifer thickness is available, this was calculated using predominantly terrain attributes. Based on the assumption that unconfined productive aquifers coincide with sediment basins below river valleys the distinction was made between (1) mountain ranges with negligible sediment thickness, consisting mainly of hard rock with secondary permeability and (2) sediment basins with thick sediment layers, presenting aquifers.

Aquifer thicknesses were then estimated as follows:

1. Mountain ranges and sediment basins were distinguished based on the difference between surface elevation and floodplain elevation. We used elevation data at $30''$ from the HydroSHEDS dataset to determine the floodplain elevation at $6'$. First, for each $6'$ cell we identified the lowest elevation at $30''$ (maximum 144 values for a cell comprising only land area) and assigned this as the floodplain elevation for the entire cell. Next, the difference between surface elevation, also taken from the HydroSHEDS database, and floodplain elevation at $6'$ was calculated. All cells with a floodplain elevation within $50\,\mathrm{m}$ below the surface level were assumed to form a sediment basin that constitutes an unconfined and

relativaly permeable aquifer (Fig. 2, top panel). These defined sediment basins included 70 % of the unconsolidated sediments mapped in the GLiM. The sediment basins consist of 56 % unconsolidated sediments, 25 % consolidated sediments and 19 % metamorphic or plutonic rocks. The latter are mainly found over the old cratons of Africa and the flat, recently glaciated areas of Laurasia.

2. By definition basins are linked to sedimentary environments in fluvial systems and deltas. Sediments are deposited perpendicular to the main gradient (constituting the transversal axis of the basin), with grain size and volumes decreasing at greater distance away from the transversal axis. Grain size also decreases along the transversal axis, distinguishing proximal (near the source of sediment) and distal parts. We assumed that gradation in grain size is captured in the GLiM but differentiation in depth is not. Instead, we used relative elevation as a measure of proximity to the river measured along the transversal axis and as an indicator of the associated depth. We standardized the relative elevation and used this to define the distribution of aquifer depths using a log-normal distribution, assuming depth is non-negative and positively skewed. In more detail, we used the following procedure:

   First, for each cell-location x belonging to the sediment basins a measure expressing the relative difference between land surface elevation and floodplain elevation was calculated:

$$F'(x) = 1 - \frac{F(x) - F_{\text{min}}}{F_{\text{max}} - F_{\text{min}}} \tag{1}$$

   where $F(x)$ is the difference of surface and floodplain elevation at location x. F_{min} and F_{max} are the minimal and maximal value, corresponding to a difference between land surface and floodplain elevation of 0 and 50 m respectively. This measure leads to a thinning layer further from the river towards the edge of the sediment basin (Fig. 2 bottom panel). $F'(x)$ can be seen as the likelihood of finding a thick sedimentary aquifer at a particular location. A map of the spatial distribution of $F'(x)$ is given in the Supplementary material, Fig. A.

Second, the associated z-score is then calculated as:

$$Z(x) = G^{-1}(F'(x)) \tag{2}$$

where $G^{-1}()$ is the inverse of the standard normal distribution.

3. Next, statistics on the thickness of unconsolidated sediments were obtained from available regional scale groundwater studies in the USA (e.g. Central Valley California, Faunt et al., 2009, Mississippi basin, Clark and Hart, 2009). As a measure of *difference between* aquifer systems, for each study the average thickness was determined resulting in a range of average thickness between 50 and 500 m. Across the delineated sediment basins (hereafter denoted as aquifers) we assume aquifer thickness to be log-normally distributed. Therefore, this distribution is described using the average thickness of the ln-transformed thickness $\overline{\ln D}$. This $\overline{\ln D}$ is chosen uniform over the globe from the range of thickness:

$$\overline{\ln D} = U(min; max). \tag{3}$$

Moreover, as a measure of *variation in thickness within* aquifers systems, an average coefficient of variation was determined from the same USA regional groundwater studies. The coefficient of variation of the ln-transformed thickness $Cv_{\overline{lnD}}$ was fixed when calculating the global distribution of aquifer thickness.

4. For each realization a spatial distribution of aquifer thickness is generated, assuming a log-normal distribution with random average $\overline{\ln D}$, sampled from $U(min; max)$ with a fixed coefficient of variation $Cv_{\overline{\ln D}}$, and using the standard normal ordinate $Z(x)$ that is based on the topographical controls within each delineated basin:

$$Y(x) = \overline{\ln D}(1 + Cv_{\overline{\ln D}} Z(x)) \tag{4}$$

$$D(x) = e^{Y(x)}. \tag{5}$$

So in this representation $Y(x)$ and $D(x)$ are random because $\overline{\ln D}$ is random, while spatial variation is determined in $Z(x)$ reflecting the likelihood of a thick aquifer. Average aquifer

thicknesses was simulated randomly from $U(50, 500)$ resulting in 100 equally likely maps of aquifer thickness. The result of the best performing run (selected after validation) is presented in Fig. 3a.

After estimating the aquifer thicknesses transmissivities were calculated. To estimate aquifer permeability at greater depth we combined the concept of exponentially decreasing permeability of the continental crust with depth (Ingebritsen and Manning, 1999) with data on near surface permeability from Gleeson et al. (2011). The permeability decline with depth is prescribed by the sediment-bedrock profile at a location, which depends strongly on terrain slope; the steeper the land, the thinner the weathered layer and the sharper the decrease in permeability with depth. This is expressed through the e-folding depth α (range and global spacial distribution of e-folding depth is given in the supplementary material, Fig. 2 and Fig. 3 and taken from Miguez-Macho et al. (2008)). With near surface permeability k_0 ($\mathrm{m\,d^{-1}}$, from Table 1) the transmissivity $T(x)$ ($\mathrm{m^2\,d^{-1}}$) over the aquifer depth $D(x)$ (m) can then be calculated as:

$$T(x) = \int_0^{D(x)} k_0 e^{\frac{-z}{\alpha}} \,\mathrm{d}z \tag{6}$$

As Eq 6. is an exponential function, permeabilities will approximate zero at greater depth.

It is assumed that conductivities are horizontally homogeneous within a hydrolithological class. The globally calculated transmissivities are presented in Fig 3b. Note that for mountain ranges low permeabilities are calculated that represent the permeabilities of the bedrock, thereby neglecting weathered regolith soils with high permeabilities that develop on the more gentle slopes. As a result perched water tables that develop in these soils are not included in the simulated lateral groundwater flow. Instead, runoff associated with these perched water tables is taken care of in the land-surface model (PCR-GLOBWB) as stormflow or interflow from the second soil reservoir. It should be recognized that our MODFLOW model is built at $6'$ and cells thus have different lengths units. To account for this a spatially variable anisotropy factor can be introduced. We have not yet implemented this option, but will do so in future work.

2.3 Boundary conditions, recharge, and drainage levels

For large lakes and the ocean a Dirichlet boundary condition was used. For the ocean the groundwater head was set at $0\,\mathrm{m}$, water levels of the lakes were set at elevation levels provided by the HydroSHEDS digital elevation map.

The steady-state groundwater recharge, shown in Fig. 4 and obtained from PCR-GLOBWB as the long-term average (for 1960-2000), was used as input for the recharge package of MODFLOW. In the MODFLOW calculation, the input value of recharge is multiplied by the MODFLOW cell dimension to get a volume per unit time, $\mathrm{L}^3\,\mathrm{T}^{-1}$. However, the input coming from our hydrological model is calculated for a geographic projected cell, thus varying surface areas. Given this fact, modifed our recharge input as follows:

$$\mathrm{RCH_{inp}} = \mathrm{RCH_{act}} \times \frac{A_{\mathrm{cell}}}{A_{\mathrm{MF}}} \tag{7}$$

where A_{cell} is the cell area of the projected cell, A_{MF} is the cell area of the MODFLOW cell, $\mathrm{RCH_{act}}$ is the groundwater recharge coming from PCR-GLOBWB (Figure 4), and $\mathrm{RCH_{inp}}$ is the modified input for the MODFLOW calculation.

We used the MODFLOW river (RIV) and drain (DRN) packages to incorporate interactions between groundwater bodies and the surface water. We distinguished three levels of groundwater-surface water interactions: (1) large river with a width $>10\,\mathrm{m}$, (2) smaller rivers, with a width $<10\,\mathrm{m}$, and (3) springs and streams higher up in river valleys.

1. For the larger rivers the interactions are governed by actual groundwater heads and surface water levels. The latter can be obtained from the long-term average naturalized river discharge, $\overline{Q_{\mathrm{chn}}}$ (calculated by PCR-GLOBWB), by using assumed channel properties. These are: channel width, W_{chn} (L), channel depth, D_{chn} (L), Manning roughness coefficient, n ($\mathrm{L}^{-1/3}\,\mathrm{T}^{-1}$), and channel longitudinal slope, Sl (–).

   The channel width was calculated using Lacey's formula (Lacey, 1930):

   $$W_{\mathrm{chn}} \approx P_{\mathrm{bkfl}} = 4.8 \times Q_{\mathrm{bkfl}}^{0.5} \tag{8}$$

where P_{bkfl} (m) is the wetted perimeter, Q_{bkfl} is the long-term averaged natural bankfull discharge ($\mathrm{m^3\,d^{-1}}$) and 4.8 ($\mathrm{s^{0.5}\,m^{-0.5}}$) is a factor (Savenije, 2003). In large natural braided rivers P_{bkfl} is slightly larger than W_{chn}. The bankflul discharge was calculated from the simulated river discharges and occurs, as a role of thumb, every 1.5 year. Combining Lacey's formula with Manning's formula (Manning, 1891) assuming a rectangular channel gives for channel depth:

$$D_{\text{chn}} = \left(\frac{n \times Q_{\text{bkfl}}^{0.5}}{4.8 \times \text{Sl}^{0.5}} \right)^{\frac{3}{5}} \tag{9}$$

By subtracting D_{chn} from surface elevation we estimated the bottom elevation of the river bed RBOT (m). The average river head HRIV (m) was subsequently calculated from the long- term average naturalized river discharge $\overline{Q_{\text{chn}}}$ using the Manning formula:

$$\text{HRIV} = \text{RBOT} + \left(\frac{n \times \overline{Q_{\text{chn}}}}{B_{\text{chn}} \times \text{Sl}^{0.5}} \right)^{\frac{3}{5}} \tag{10}$$

The RBOT and the HRIV were used as input for the RIV package in MODFLOW to calculate the flow between the river and aquifer: Q_{riv} ($\mathrm{m^3\,d^{-1}}$). If the head in the cell connected to the river drops below the bottom of the river bed, water enters the groundwater system from the river at a constant rate. If the head is above the bottom of the river bed, water will either enter or leave the aquifer system depending on whether the head is above or below the river head. Q_{riv} is positive when water from the river enters the aquifer and is calculated as follows:

$$Q_{\text{riv}} = \begin{cases} c \times (\text{HRIV} - h) & \text{if } h > \text{RBOT} \\ c \times (\text{HRIV} - \text{RBOT}) & \text{if } h \leq \text{RBOT} \end{cases} \tag{11}$$

where h is groundwater head (m), and c is a conductance ($\mathrm{m^2\,d^{-1}}$) calculated as:

$$c = \frac{1}{\text{BRES}} \times P_{\text{chn}} \times L_{\text{chn}} \tag{12}$$

where BRES is bed resistance (d, taken 1 day here), L_{chn} (m) is the channel length (approximated the diagonal cell length as tortuosity here). The river package was used only for cells with large rivers, i.e. $W_{\text{chn}} \geq 10\,\text{m}$.

2. To simulate smaller rivers, $W_{\text{chn}} < 10\,\text{m}$, the DRN package was used. Water can only leave the groundwater system through the drain when head gets above the drainage level which was taken equal to the surface elevation, DEM. The drainage Q_{drn} ($\text{m}^3\,\text{d}^{-1}$) is then calculated as follows:

$$Q_{\text{drn}} = \begin{cases} c \times (\text{DEM} - h) & \text{if } h > \text{DEM} \\ c \times 0 & \text{if } h \leq \text{DEM} \end{cases}. \tag{13}$$

Figure 4 shows larger rivers and active smaller rivers for Europe and Africa.

3. Q_{riv} and Q_{drn} are the main components of the baseflow Q_{bf}. However, at 6′ resolution the main stream is insufficient to represent truthfully all locations within a cell where groundwater levels intersect the terrain and additional drainage is needed to represent local sags, springs, and streams higher up in valleys in mountainous areas. To resolve this issue, we assumed that groundwater above the floodplain level can be tapped by local springs which were presented by means of a linear storage-outflow relationship. Thus, baseflow was simulated as:

$$Q_{\text{bf}} = -(Q_{\text{riv}} + Q_{\text{drn}}) + (JS_{3,\text{flp}}) \tag{14}$$

where $S_{3,\text{flp}}$ (m) is the groundwater storage above the floodplain as obtained from PCR-GLOBWB and J (d^{-1}) is a recession coefficient parameterized based on Kraaijenhof van der Leur (1958):

$$J = \frac{\pi T}{4 S_y L^2} \tag{15}$$

where T ($\text{m}^2\,\text{d}^{-1}$) is the transmissivity as used in the groundwater model, S_y is the storage coefficient assumed for each hydrolithological category (see Table 1), and L is the average

distance between streams and rivers as obtained from the stream density (see van Beek et al. (2011)).

2.4 Sensitivity analysis of aquifer properties and recharge

In groundwater modelling the transmissivity and groundwater recharge are important parameters and subject to large uncertainty. In this study we investigated the sensitivity of the model outcome to changes in the aquifer parameters (conductivity, thickness) and recharge.

For each parameter a Monte Carlo simulation of 100 samples was performed. This simulation followed a log-normal distribution for layer thickness and saturated conductivity. For groundwater recharge a normal distribution was used. For layer thickness, mean and standard deviation were obtained by combining several case studies of the USA and extrapolating this globally (see section 2.2, equations 1-5). Means and standard deviations of saturated conductivities per hydrolithological class were taken from Gleeson et al. (2011) (see Table 1). Mean and standard deviations for groundwater recharge were taken for the PCR-GLOBWB sensitivity study of Wada et al. (2014).

The variation in groundwater depth caused by changing one parameter was evaluated by calculating maps coefficients of variation. To obtain the uncertainty from the combination of these parameters, for each parameter 10 evenly distributed quantiles were determined and combined into 1000 parameter sets to run the model with. Again variation in groundwater depth was evaluated by calculating maps coefficients of variation.

2.5 Validation of groundwater depths

Simulated groundwater depths were validated against a compilation of reported piezometer data (Fan et al., 2013). The average of the reported data was used if more than one observation was available within a $6'$ cell, giving a total of 65 303 cells with observations worldwide. The water table head, instead of depth, was evaluated as it measures the potential energy that drives flow and is therefore physically more meaningful. The coefficient of determination (R^2) and regres-

sion coefficient (α) were calculated for every run. Residuals (*res*) were calculated as simulated heads minus observed heads and maps are presented.

2.6 Simulating flowpaths

Particle tracking, using MODPATH (Pollock, 1994), was included to track flowpaths and estimate travel times of groundwater flows. For this simulation cell-to-cell flux densities calculated by MODFLOW were used. A flowpath is computed by tracking the particle from one cell to the next until it reaches a boundary or sink. It shows the actual path through the subsoil that the groundwater follows from the location of infiltration towards the location of drainage. In our case the particle was stopped when it reached the ocean, a lake, or the local drainage (rivers or drains). It provides insights in regional scale groundwater movements and groundwater age, indicating areas where lateral groundwater flows are significant and inter-basin groundwater flows are important. These inter-basin groundwater flows positively affect water budgets in neighbouring river basins or recharge to the aquifer system. Results are presented for Europe and Africa, showing paths and travel times.

3 Results and discussion

3.1 Sensitivity analysis

Figure 5a shows the coefficient of variation (CV) of calculated groundwater depths with changing parameter settings for saturated conductivity, aquifer thickness, and recharge. Overall CVs are small. Higher CVs are found for the Sahara and Australian desert, where recharge is low, transmissivities are high, and groundwater levels become disconnected from the surface. This emphasizes the influence of regional scale lateral flow in these areas. Higher variations are also found for areas with shallow groundwater tables and higher transmissivities and recharge, like the Amazon and Indus basin.

Figure 5b shows the CVs of calculated groundwater depths when only saturated conductivity is considered. It can bee seen that these CVs are very similar to the run with three changing

parameters, illustrating that saturated conductivity is predominantly controlling groundwater depths. This is expected as the standard deviation of saturated conductivity is large for several hydrolitological classes (Table 1), changing saturated conductivity by orders of magnitude. In general a higher saturated conductivity leads to lower water tables and more significant regional groundwater flow, and vice versa.

The other two parameters, aquifer thickness and groundwater recharge, are of lower importance. Although different thickness do change transmissivities, impact on calculated groundwater depths is small. Also, the effect of changing groundwater recharge is small. This is the direct result of the small relative uncertainty compared to hydraulic conductivity. Beside this, drainage is self-limiting; as recharge increases, the water table rises and the hydraulic gradient is steepened, accelerating drainage and lowering the water table. This dampens the water table sensitivity to recharge uncertainties.

3.2 Validation of groundwater heads

Simulated groundwater heads were compared to piezometer observations. A scatter plot of the best performing run (after changing three parameters) is presented in Fig. 6 and spatial patterns are presented in Fig. 7. It should be mentioned here that for most regions of the world no observation data are available or are incomplete (i.e. no elevation measurement, see supplementary material Fig. 4). While interpreting the results it should be noted that observation locations are biased towards river valleys, coastal ribbons, and the areas where productive aquifers occur. Also, observations are taken at a certain moment in time, and thus are liable to seasonal effects and drawdown as a result of abstractions, while simulated groundwater heads represent the steady state average. Beside this, for the mountain ranges it is likely that observations are located in small mountain valleys with shallow water tables, partly from infiltrating streams. Our grid resolution is too coarse to capture these small-scale features. Also, occasionally observations of perched water tables in hill slopes are included. These perched groundwater tables are not described by our large-scale groundwater model, but captured in the land surface model as interflow.

For all runs the computed coefficient-of-determination (R^2) was calculated and found to fall between 0.75 and 0.87. For the 10 best performing runs it ranges between 0.85 and 0.87. The scatter of the best performing run is given in Fig. 6. The presented scatter and statistics of R^2 and regression coefficient α in Fig. 6 show the model performance is good. However, the scatter also shows a strong underestimation of groundwater heads, especially for the higher values (i.e. higher elevated areas). As it is expected that at higher and steeper terrains observations are most likely different from the simulated regional scale groundwater heads (as described above), we looked at sediment basins and mountain ranges separately, presented in red and blue respectively. The R^2 for sediment basins ranges between 0.90 and 0.95, and for the 10 best performing runs between 0.945 and 0.946.

In Fig. 7 the spatial distribution of the residuals of groundwater depth and corresponding histograms are shown for Europe and the USA. The figures confirm that in general groundwater depths are overestimated. This overestimation is largest for higher elevated areas, such as the Rocky Mountains, and lower for flatter areas, such as the Mississippi embayment. The histograms show that larger residuals are mainly found for areas where also deeper groundwater depths are observed. This means that, although the absolute error is large, the relative error is small and deep simulated groundwater levels do correspond with deep observed groundwater levels. Also, smaller residuals are found where shallow groundwater tables are observed.

3.3 Global groundwater depth map

Figure 8 shows for the best performing run the simulated steady-state groundwater table depths at its natural state (without pumping), in meter below the land surface (result of the best performing run).

General patterns in water table depths can be identified. At the global scale, sea level is the main control of groundwater depths. Throughout the entire coastal ribbon shallow groundwater tables occur. These areas expand where flat coastal plains meet the sea, including major river basins like Mississippi, Indus, and large wetlands. At the regional scale, recharge is the main control in combination with scale topography. For regions with high groundwater recharge rates shallow groundwater tables are simulated, for example the tropical swamps of the Amazone.

The influence of the regional topography is also evident in the central Amazon and for the flat lowlands of South America as these regions receive water from elevated areas.

Regions with low recharge rates correspond with deep groundwater where groundwater head gets disconnected from the local topography. The great deserts stand out (hyper-arid regions dotted in Fig. 8). Also for the mountain ranges of the world deep groundwater tables are simulated. As stated before, small local valleys with higher local groundwater tables are not captured by the model due to the used grid resolution. The mountainous regions where local and perched water tables are likely to occur are masked in the figure with a semi-transparent layer.

3.4 Groundwater flow paths and travel time

Figure 9 shows the simulated large-scale flowpaths for Europe and Africa where different colors indicate the simulated travel times. These figures show both short and long inter-basin flowpaths, that are stopped when they reach the local drainage, such as a lake or the ocean. Long flowpaths are for example found in East-Europe, where paths end as submarine groundwater discharge. Also, for Africa long flow paths are evident for the desert area. The flowpath simulations shows that especially for sediment areas, inter-basin groundwater flow is important and significant at least at longer time scales. It should be noted that these are larger-scale flowpaths associated with the scale of the model. Obviously, superimposed on these areas subregional to local-scale flowpaths of shallow groundwater systems exist not captured by our model (Toth, 1963).

4 Conclusions

In this paper a global scale groundwater model of an upper unconfined aquifer layer is presented. A feasible and relatively simple method is introduced to overcome the limited information available for aquifer parameterization; available global datasets for lithology and saturated conductivity were used such that the parameterization method can be expanded to data poor environments.

By applying this method we are able to produce a global picture of water table depths at fine resolution ($6'$) within acceptable accuracy in many part of the world, especially for sediment basins ($R^2 = 0.95$ and $\alpha = 0.84$). The sediment basins are specific areas of interest, as these include the major aquifer systems of the world (e.g. Indus, Ganges, High Plains). For the higher and steeper terrain groundwater depths are in general underestimated compared to observations, likely because perched water tables on hillsides, are not included in the groundwater model but are present in the observations. Additionally, the model resolution and the aquifer property estimation are still too coarse to capture shallow water tables in small sediment pockets in small mountain valleys.

The results presented in this study confirm the relevance of taking lateral groundwater flow into account in global scale hydrological models. Short and long inter-basin flowpaths are simulated. The latter can be of major importance to sustain river baseflow in times of droughts supporting ecosystems and wetlands and increasing surface water availability for human water use. Also, inter-basin groundwater flows can act as additional recharge to large aquifer systems, thereby increasing water availability in these aquifers.

Obviously the model presented here must be considered as a first-order attempt towards global groundwater modelling and consequently has a number of limitations that prevent it from simulating groundwater dynamics completely truthfully.

Firstly, the model simulates a natural dynamic steady-state; it does not provide any information about groundwater fluctuations caused by climate (seasonal and inter-annual) or human water use. Obviously, as we have estimated specific yield as well, extension to transient simulations is straightforward and will be attempted in a next study.

Secondly, only one unconfined layer is modelled here, while in reality, multi-layered aquifers including unconsolidated and consolidated layers can be present. Before we can include human groundwater use globally, these multi-layered aquifers should be included in the model as this holds vital information on the accessibility and quality of global groundwater resources. However, the information on these aspects is sparse and incomplete.

Thirdly, capillary rise of the water table into the soil has not yet been implemented, although several studies have pointed out that it can affect soil moisture, evaporation, or even precipitation

(e.g. Bierkens and van den Hurk, 2007; Fan et al., 2013; Lam et al., 2011). Further, there is no dynamic interaction between groundwater and surface water, as the drainage level of rivers does not change over time.

That being said, our model has the ability to capture the large scale distribution of groundwater levels and as such can serve as a starting point leading to a tool to assess groundwater level fluctuations and their sensitivity to human water intervention and climate.

The next step of this work will be to expand the current aquifer schematization with multi-layered and confined aquifer systems. The model will become transient and fully coupled to the land-surface model in order to incorporate capillary rise to the soil moisture and link river dynamics with groundwater. Human water use will be included as well. The goal will be to represent the impact of human water use on groundwater dynamics and river discharges. It will show where and when limits of groundwater abstractions will be reached. This is vital information needed to ensure sustainable and efficient groundwater use, particularly for semi-arid regions where groundwater demand will intensify due to the increase of drought frequency and duration, combined with population growth, expansion of irrigation areas, and rising standard of living.

Appendix A

Supplementary material

Figure 10 here

e-folding depth

The near surface permeability is described by the sediment- bedrock profile at a location, which depends strongly on terrain slope; the steeper the land, the thinner the regolith and the sharper the decrease in permeability with depth (e.g. Miguez-Macho et al. (2008). This is expressed through the e-folding depth. The range of the e- folding depth (α) is given in the graph below, and its spatial distribution in the map below.

Figure 11 here

Figure 12 here
Figure 13 here

Acknowledgements. This study was funded by the Netherlands Organization for Scientific Research (NWO) in the project Planetary Boundaries Fresh Water Cycle. We also thank Peter Vermeulen for his assistance with iMOD, used for the particle tracking as presented in this paper.

References

references

Beven, K. J. and Kirkby, M. J.: Considerations in the development and validation of a simple physically based, variable contributing area model of catchment hydrology, in: Surface and subsurface hydrology, Proc. Fort Collins 3rd international hydrology symposium, July 1977, Fort Collins, 23–36, 1979.

Bierkens, M. F. P. and van den Hurk, B. J. J. M.: Groundwater convergence as a possible mechanism for multi-year persistence in rainfall, Geophys. Res. Lett., 34, L02402, doi:http://dx.doi.org/10.1029/2006GL02839610.1029/2006GL028396, 2007.

Clark, B. and Hart, R.: The Mississippi Embayment Regional Aquifer Study (MERAS): Documentation of a groundwater-flow model contructed to assess water Availability in the Mississippi Embayment, Tech. Rep. 5172, US Geological Survey Scientific Investigations Report, US Geological Survey, Reston, Virginia, 2009.

de Graaf, I. E. M., van Beek, L. P. H., Wada, Y., and Bierkens, M. F. P.: Dynamic attribution of global water demand to surface water and groundwater resources: effects of abstractions and return flows on river discharges, Adv. Water Resour., 64, 21–33, doi:http://dx.doi.org/10.1016/j.advwatres.2013.12.00210.1016/j.advwatres.2013.12.002, 2014.

Dee, D., Uppala, S., Simmons, A., Berrisford, P., Poli, P., Kobayashi, S., Andrae, U., Balmaseda, M., Balsamo, G., Bauer, P., Bechtold, P., Beljaars, A., van de Berg, L., Bidlot, J., Bormann, N., Delsol, C., Dragani, R., Fuentes, M., Geer, A., Haimberger, L., Healy, S., Hersbach, H., Hólm, E., Isaksen, L., Kållberg, P., Köhler, M., Matricardi, M., Mcnally, A., Monge-Sanz, B., Morcrette, J.-J., Park, B.-K., Peubey, C., de Rosnay, P., Tavolato, C., Thépaut, J.-N., and Vitart, F.: The ERA-Interim reanalysis: configuration and performance of the data assimilation system, Q. J. Roy. Meteorol. Soc., 137, 553–597, 2011.

Dürr, H. H., Meybeck, M., and Dürr, S. H.: Lithologic composition of the Earth's continental surfaces derived from a new digital map emphasizing riverine material transfer, Global Biogeochem. Cy., 19, GB4S10, doi:http://dx.doi.org/10.1029/2005GB00251510.1029/2005GB002515, 2005.

Fan, Y., Miguez-Macho, G., Weaver, C. P., Walko, R., and Robock, A.: Incorporating water table dynamics in climate modeling: 1. Water table observations and equilibrium water table simulations, J. Geophys. Res.-Atmos., 112, D10125, doi:http://dx.doi.org/10.1029/2006JD00811110.1029/2006JD008111, 2007.

Fan, Y., Li, H., and Miguez-Macho, G.: Global patterns of groundwater table depth, Science, 339, 940–943, doi:http://dx.doi.org/10.1126/science.122988110.1126/science.1229881, 2013.

Faunt, C. C. (Ed.): Groundwater availability of the Central Valley Aquifer, US Geological Survey Professional Paper 1766, US Geological Survey, California, p. 255, 2009.

Gleeson, T., Smith, L., Moosdorf, N., Hartmann, J., Dürr, H. H., Manning, A. H., van Beek, L. P. H., and Jellinek, A. M.: Mapping permeability over the surface of the Earth, Geophys. Res. Lett., 38, L02401, doi:http://dx.doi.org/10.1029/2010GL04556510.1029/2010GL045565, 2011.

Gleeson, T., Wada, Y., Bierkens, M. F. P., and van Beek, L. P. H.: Water balance of global aquifers revealed by groundwater footprint, Nature, 488, 197-200, doi:http://dx.doi.org/10.1038/nature1129510.1038/nature11295, 2012.

Gleeson, T., Moosdorf, N., Hartmann, J., and van Beek, L. P. H.: A glimpse beneath earth's surface: GLobal HYdrogeological MaPS (GLHYMPS) of permeability and porosity, Geophys. Res. Lett., 41, 3891-3898, doi:http://dx.doi.org/10.1002/2014GL05985610.1002/2014GL059856, 2014

, Derivation of global GCM boundary conditions from 1 km land use satellite data, Rep. 289. Tech. Rep., Max Planck Institude for Meteorology, Hamburg, Germany.

Hartmann, J. and Moosdorf, N.: The new global lithological map database GLiM: a representation of rock properties at the Earth surface, Geochem. Geophy. Geosy., 13, Q12004, doi:http://dx.doi.org/10.1029/2012GC00437010.1029/2012GC004370, 2012.

Ingebritsen, S. and Manning, C.: Geological implications of a permeability-depth curve for the continental crust, Geology, 27, 1107–1110, doi:http://dx.doi.org/10.1130/0091-7613(1999)027%3C1107:GIOAPD%3E2.3.CO;210.1130/0091-7613(1999)027<1107:GIOAPD>2.3.CO;2, 1999.

Konikow, L. F.: Contribution of global groundwwater depletion since 1900 to sea-level rise,geophysical research letters, 38, L17401, doi:http://dx.doi.org/10.1029/2011GL04860410.1029/2011GL048604,2011.

Kraaijenhof van der Leur, D.: A study of non-steady grounground flow with special reference to a reservoir coefficient, de ingenieur, 70, 87–94, 1958.

Krakauer, N. Y., Li, H., and Fan, Y.: Groundwater flow across spatial scales: importance for climate modeling, Environ. Res. Lett, 9,034003, doi:http://dx.doi.org/10.1088/1748-9326/9/3/03400310.1088/1748-9326/9/3/034003,2014.

Lacey, G.: Stable cchannel in alluvium, P. I. Civ. Eng., 229, 259–292, 1930.

Lam, A., Karssenberg, D., van den Hurk, B. J. J. M., and Bierkens, M. F. P.: Spatial and temporal connections in groundwater contribution to evaporation, Hydrol. Earth Syst. Sci., 15, 2621–2630, doi:http://dx.doi.org/10.5194/hess-15-2621-201110.5194/hess-15-2621-2011, 2011.

Manning, R.: On the flow of water in open cchannel and pipes, Transactions of Institution of Civil Engineers of Ireland, Dublin, 161–207, 1891.

McDonald, M. G. and Harbaugh, A. W.: MODFLOW-2000, the US Geological Survey modular ground-water model – User guide to modularmodular concepts and the Ground-Water Flow Process, Tech. rep., US Geological Survey, Reston, Virginia, 2000.

Miguez-Macho, G., Li, H., and Fan, Y.: Simulated water table and soil moisture climatology over north america, B. Am. Meteorol. Soc., 89, 663–672, doi:http://dx.doi.org/10.1175/BAMS-89-5-66310.1175/BAMS-89-5-663, 2008.

Mitchell, T. D. and Jones, P. D.: An improved method of constructing a database of monthly climate observations and associated high-resolution grids, Int. J. Climatol., 25, 693–712, doi:http://dx.doi.org/10.1002/joc.118110.1002/joc.1181, 2005.

Pollock, D.: User's Guide for MODPATH/MODPATH-PLOT, version 3: A particle tracking post-processing package for MODFLOW, the US Geological Survey finite-difference groundwater flow model, Tech. rep., US Geological Survey Open-File Report 94-464, US Geological Survey, Reston, Virginia, 1994.

Savenije, H. H.: The width of a bankfull channel; Lacey's formula explained, J. Hydrol., 276, 176–183, doi:http://dx.doi.org/10.1016/S0022-1694(03)00069-610.1016/S0022-1694(03)00069-6, 2003.

Schaller, M. F. and Fan, Y.: River basins as groundwater exporters and importers: implications for water cycle and climate modeling, J. Geophys. Res.-Atmos., 114, D04103, doi:http://dx.doi.org/10.1029/2008JD01063610.1029/2008JD010636, 2009.

Schmitz, O., Karssenberg, D., van Deursen, W., and Wesseling, C.: Linking external components to spatio-temporal modeling framework: coupling MODLFW and PCRaster, Environ. Modell. Softw., 24, 1088–1099, doi:http://dx.doi.org/10.1016/j.envsoft.2009.02.01810.1016/j.envsoft.2009.02.018, 2009.

Summerfield, M. and Hulton, N.: Natural controls of fluvial denudation rates in major world drainage basins, J. Geophys. Res., 99, 13871–13883, 1994.

Sutanudjaja, E. H., van Beek, L. P. H., de Jong, S. M., van Geer, F. C., and Bierkens, M. F. P.: Large-scale groundwater modeling using global datasets: a test case for the Rhine-Meuse basin, Hydrol. Earth Syst. Sci., 15, 2913–2935, doi:http://dx.doi.org/10.5194/hess-15-2913-201110.5194/hess-15-2913-2011, 2011.

Sutanudjaja. E. H.,van Beek, L. P. H., de Jong, S. M., van Geer, F. C., and Bierkens, M. F. P.: Calibrating a large-extent high-resolution coupled groundwater-land surface model using soil moisture and discharge data, Water Resourc. Res.,50,687-705, doi:http://dx.doi.org/10.1002/2013WR01380710.1002/2013WR013807,2014.

Todini, T.: The arno rainfall-runoff model. J. Hydrol. 175, 339-382, 1996.

Toth, J.: A theoretical analysis of groundwaterflow in small drainage basins, J. Geophys. Res., 68,16,2156-2202,doi:http://dx.doi.org/10.1029/ JZ068i016p0479510.1029/ JZ068i016p04795,1963.

Uppala, S. M., Kållberg, P. W., Simmons, A. J., Andrae, U., Bechtold, V. D. C., Fiorino, M., Gibson, J. K., Haseler, J., Hernandez, A., Kelly, G. A., Li, X., Onogi, K., Saarinen, S., Sokka, N., Allan, R. P., Andersson, E., Arpe, K., Balmaseda, M. A., Beljaars, A. C. M., Berg, L. V. D., Bidlot, J., Bormann, N., Caires, S., Chevallier, F., Dethof, A., Dragosavac, M., Fisher, M., Fuentes, M., Hagemann, S., Hólm, E., Hoskins, B. J., Isaksen, L., Janssen, P. A. E. M., Jenne, R., Mcnally, A. P., Mahfouf, J.-F., Morcrette, J.-J., Rayner, N. A., Saunders, R. W., Simon, P., Sterl, A., Trenberth, K. E., Untch, A., Vasiljevic, D., Viterbo, P., and Woollen, J.: The ERA-40 re-analysis, Q. J. Roy. Meteorol. Soc., 131, 2961–3012, doi:http://dx.doi.org/10.1256/qj.04.17610.1256/qj.04.176, 2005.

van Beek, L. P. H., Wada, Y., and Bierkens, M. F. P.: Global monthly water stress: 1. Water balance and water availability, Water Resour. Res., 47, W07517, doi:http://dx.doi.org/10.1029/2010WR00979110.1029/2010WR009791, 2011.

Vergnes, J.-P., Decharme, B., Alkama, R., Martin, E., Habets, F., and Douville, H.: A simple groundwater scheme for hydrological and climate applications: description and offline evaluation over france, J. Hydrometeorol., 13, 1149–1171, doi:http://dx.doi.org/10.1175/JHM-D-11-0149.110.1175/JHM-D-11-0149.1, 2012.

Wada, Y., Wisser, D., and Bierkens, M. F. P.: Global modeling of withdrawal, allocation and consumptive use of surface water and groundwater resources, Earth Syst. Dynam., 5, 15–40, doi:http://dx.doi.org/10.5194/esd-5-15-201410.5194/esd-5-15-2014, 2014.

Wood, E. F., Roundy, J. K., Troy, T. J., van Beek, R., Bierkens, M., Blyth, E., de Roo, A., Döll, P., Ek, M., Famiglietti, J., Gochis, D., van de Giesen, N., Houser, P., Jaffe, P., Kollet, S., Lehner, B.,

Lettenmaier, D. P., Peters-Lidard, C. D., Sivapalan, M., Sheffield, J., Wade, A. J., and Whitehead, P.: Reply to comment by Keith, J. Beven and Hannah, L. Cloke on "Hyperresolution global land surface modeling: Meeting a grand challenge for monitoring Earth's terrestrial water", Water Resour. Res., 48, W01802, doi:http://dx.doi.org/10.1029/2011WR01120210.1029/2011WR011202, 2012.

Table 1. Lithologic and hydrolihologic categories.
table

Lithologic categories[a]	Hydrolithologic categories[b]	$\log k\ \mu_{\text{geo}}\ [\text{m}^2]$[b]	$\sigma\ [\text{m}^2]$[b]	$S_y\ [\text{m/m}]$[c]
Unconsolidated sediments	unconsolidated	−13.0	2.0	0.235
	c.g. unconsolidated	−10.9	1.2	0.360
	f.g. unconsolidated	−14.0	1.8	0.110
Siliciclastic sediments	siliciclastic sedimentary	−15.2	2.5	0.055
	c.g. siliciclastic sedimentary	−12.5	0.9	0.100
	f.g. siliciclastic sedimentary	−16.5	1.7	0.010
Mixed sedimentary rocks Carbonate sedimentary rocks Evaporites	Carbonate	−11.8	1.5	0.140
Acid volcanic rocks Intermediate volcanic rocks Basic volcanic rocks	Crystalline	−14.1	1.5	0.010
Acid plutonic rocks Intermediate plutonic rocks Basic plutonc rocks pyroclastics metamorphic	Volcanic	−12.5	1.8	0.050
water bodies Ice and Glaciers	not assigned	–	–	–

[a] Hartmann and Moosdorf (2012).
[b] Based on Gleeson et al. (2011), $\log k\ \mu_{\text{geo}}$ is the geometric mean logarithmic permeability; σ is the standard deviation; f.g. and c.g. are fine-grained and coarse-grained, respectivaly.
[c] S_y is the storage coefficient, average per category.

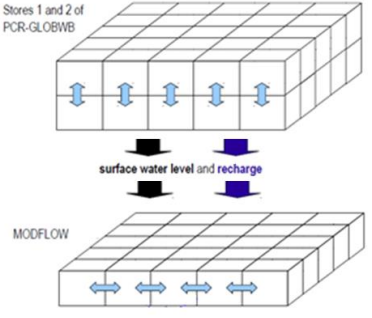

Fig. 1. Model structure used to couple the land-surface model PCR-GLOBWB with the groundwater model MODFLOW: first average annual net recharge and average annual channel discharge is calculated with PCR-GLOBWB. The latter is translated into surface water levels. Both recharge and surface water levels are used to force MODFLOW (after Sutanudjaja et al., 2011).
figure

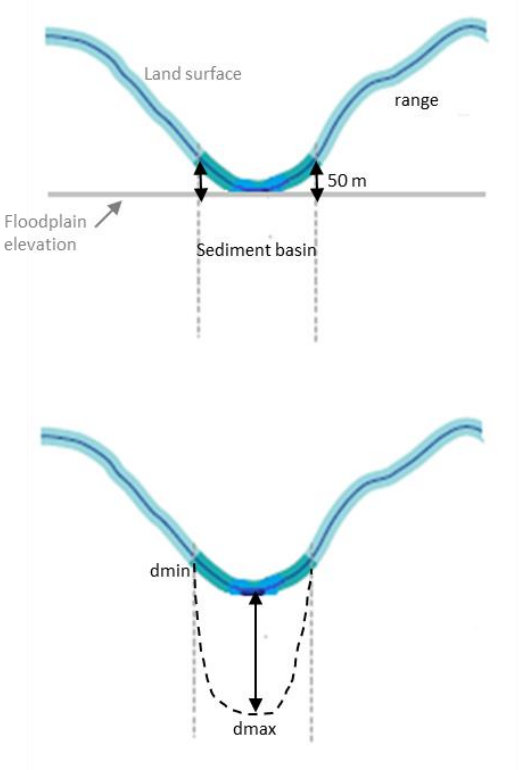

Fig. 2. (top) definition of sediment basins and mountain ranges, based on terrain attributes (land surface elevation and floodplain elevation). (bottom) estimation of aquifer thickness.

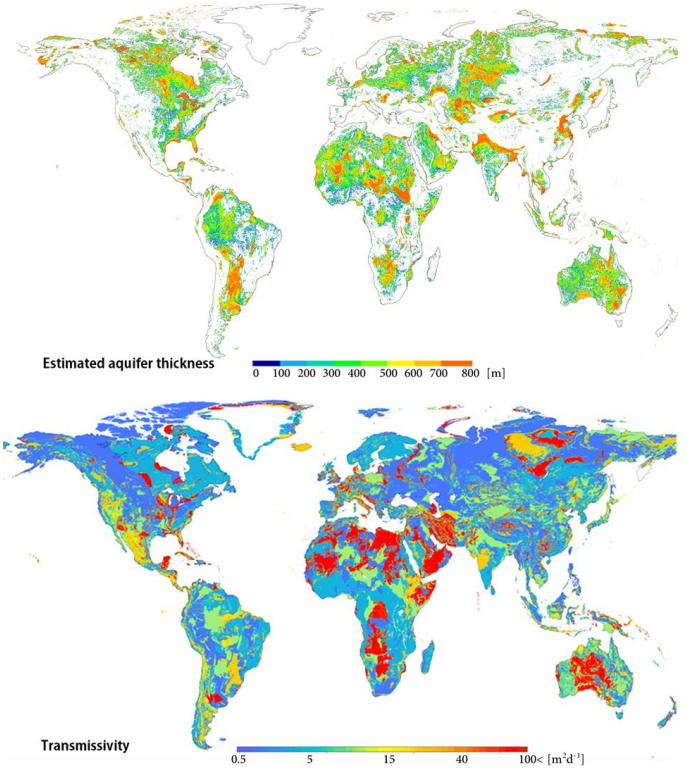

Fig. 3. Calculated aquifer thickness and tranmissivities.

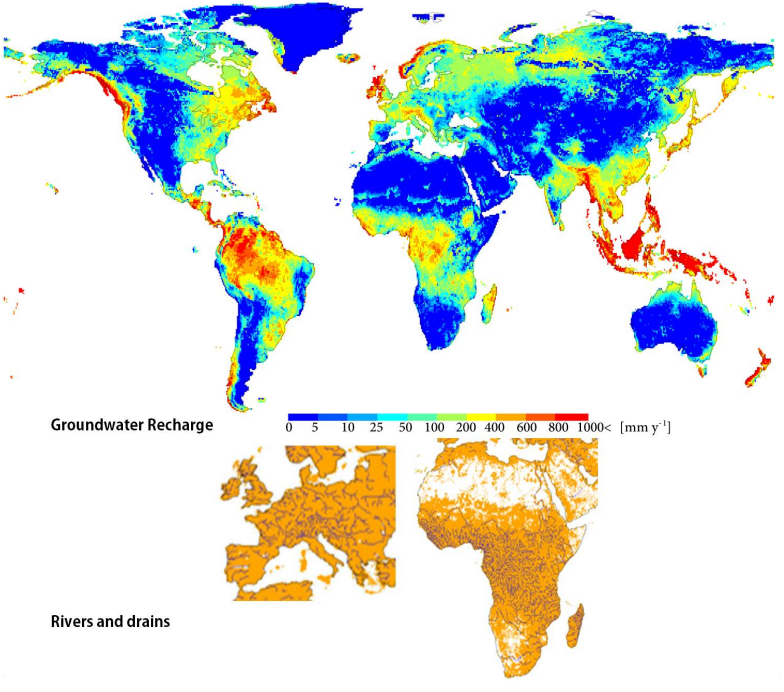

Fig. 4. (top) Steady-state recharge input as obtained from averaging PCR-GLOBWB recharge output over the period 1957-2002. (bottom) The hydrography of the imposed streamnetwork is superimposed: large rivers, with widths $>$10 m (blue) and smaller rivers, with widths 10 m (orange).

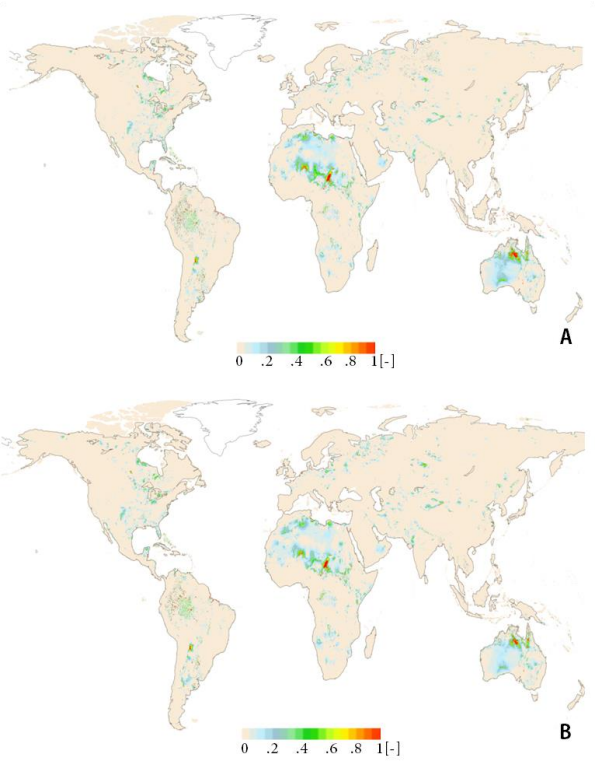

Fig. 5. Coefficient of variation of groundwater depth: (A) of 1000 runs with different parameter settings for aquifer thickness, saturated conductivity, and groundwater recharge; (B) of 100 runs with different parameter settings for saturated conductivity, other parameters remaining fixed.

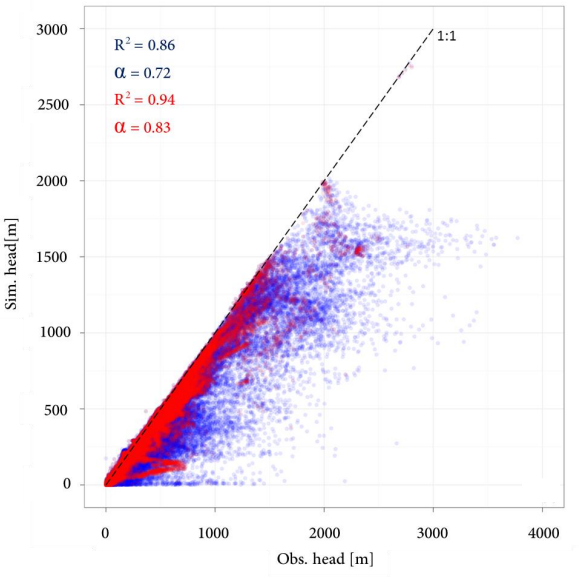

Fig. 6. Scatter plot of observed heads against simulated heads for sediment basins (red) and mountain ranges (blue).

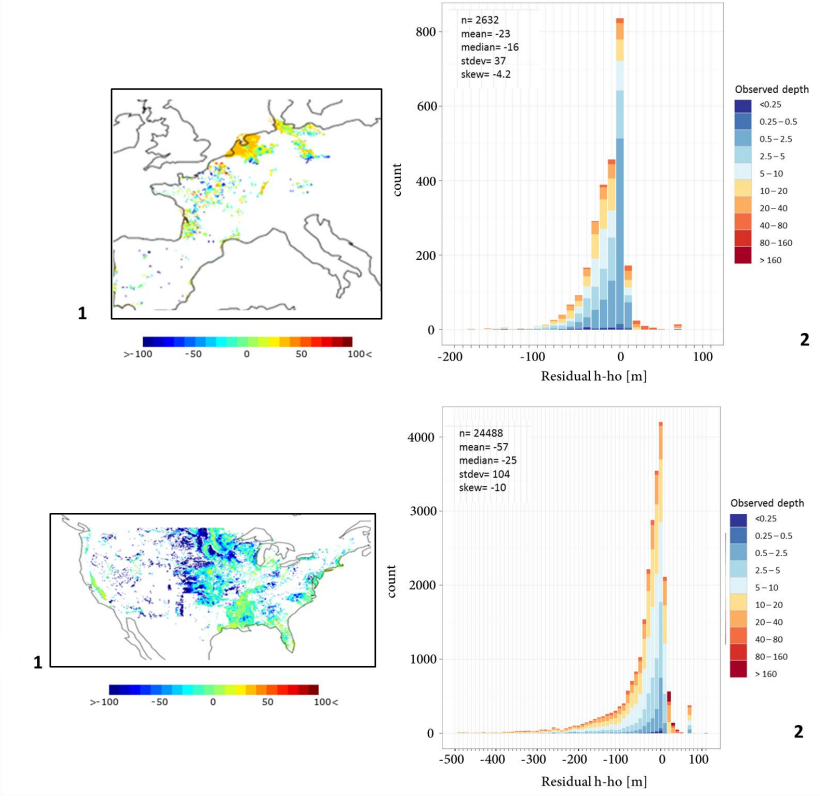

Fig. 7. Maps of residuals for NW-Europe and USA. (1) residuals and (2) histograms of residuals. Each bar in the histogram is clustered based on observed on classified groundwater depths.

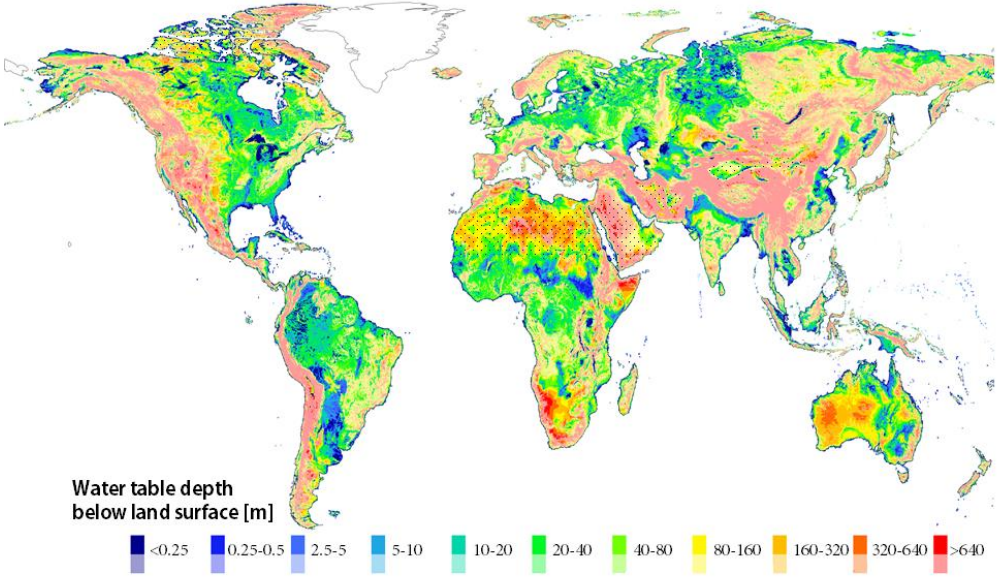

Fig. 8. Simulated water table depth in meters below the land surface. The result of a steady-state natural run, using the best estimated parameter set. Semi-transparant colours indicate deep groundwater regions where most likely more shallow perched and local water tables not captured by the model. Dotted areas indicate hyper-arid zones, distinguished at the grid resolution. White areas indicate no-data values.

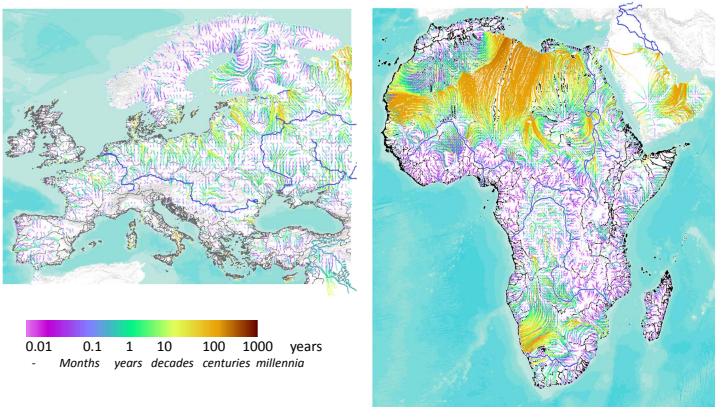

Fig. 9. Flow paths simulated for NW-Europe and Africa, underlain by river basin boundaries, overlain with major rivers.

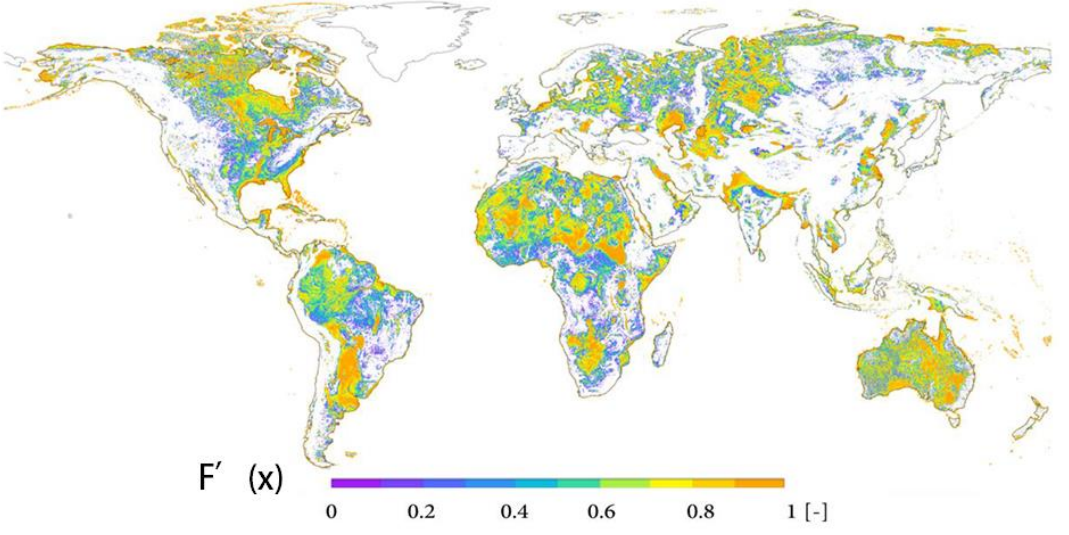

Fig. 10. Spatial distribution of $F'(x)$, representing the likelihood of finding a thick aquifer.

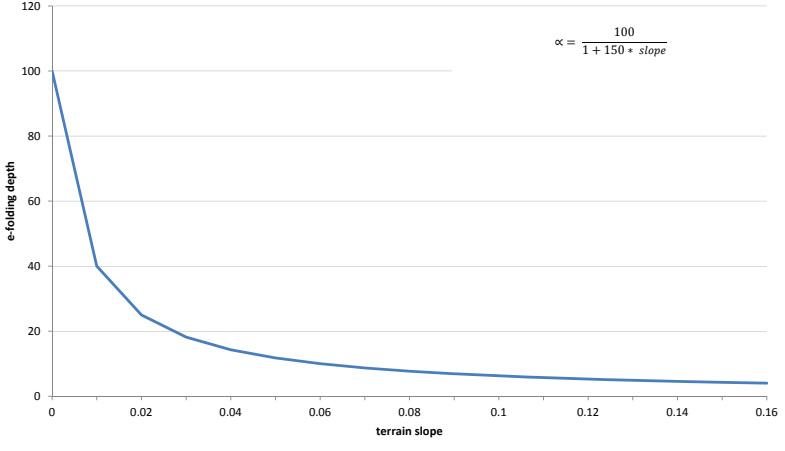

Fig. 11. e-folding depth as a function of terrain slope, using constants of Miguez-Macho et al. (2008).

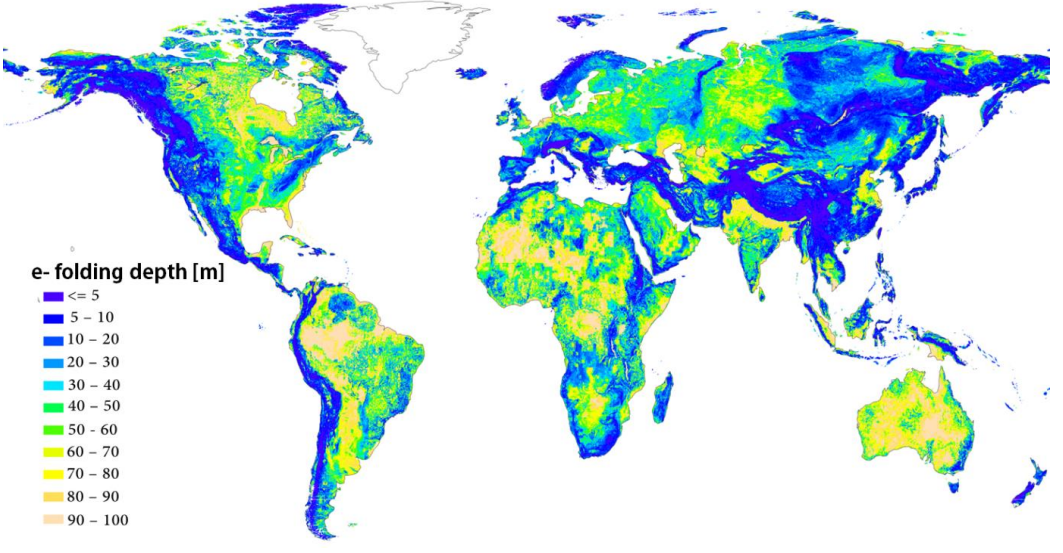

Fig. 12. e-folding depth.

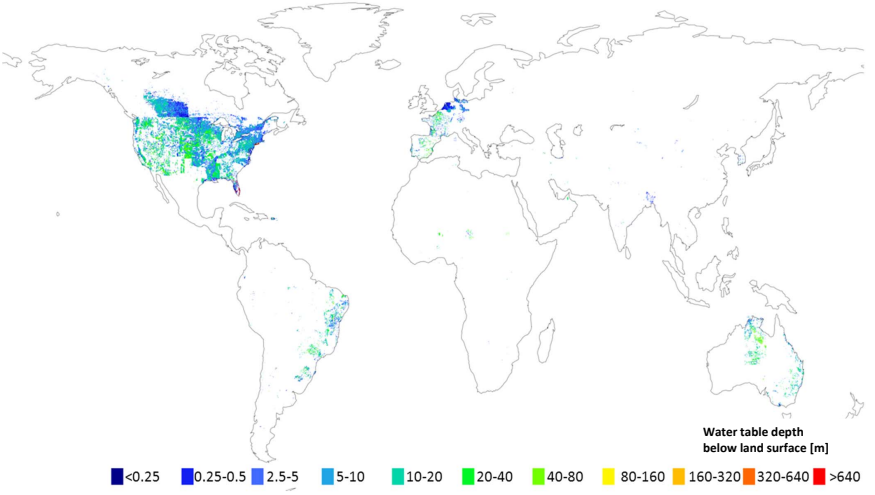

Fig. 13. global piezometer observations; groundwater depths in meters below land-surface (from Fan et al. (2013).